PAPER

Enhancement of Ce₁₋ₓSnₓO₂ support in LaMnO₃ for the catalytic oxidation and adsorption of elemental mercury†

Haomiao Xu,[a] Yongpeng Ma,[b] Songjian Zhao,[a] Wenjun Huang,[a] Zan Qu[a] and Naiqiang Yan*[a]

Mn-based perovskite oxide was used as the active site for elemental mercury (Hg^0) removal from coal-fired flue gas. $Ce_{1-x}Sn_xO_2$ binary oxides were selected as the catalyst supports for $LaMnO_3$ to enhance the catalytic oxidation and adsorption performance. $Ce_{0.7}Sn_{0.3}O_2$ had the best Hg^0 removal performance among the as-prepared $Ce_{1-x}Sn_xO_2$ binary oxides; the Hg^0 removal efficiency was 95.2% at 350 °C. $LaMnO_3$ had better performance at low temperatures (<200 °C). $LaMnO_3/Ce_{0.7}Sn_{0.3}O_2$ enlarged the reaction temperature window and enhanced the Hg^0 removal efficiencies. The correlation between the physicochemical properties and the catalytic removal performance was investigated by XRD, BET surface area measurements, Raman spectroscopy, H_2-TPR and XPS analysis. With the addition of Ce–Sn binary oxides as catalyst support, the surface areas of $LaMnO_3$ was enlarged, the reducibility was enhanced and the oxygen mobility was improved. In addition, the Hg^0 removal mechanism was illustrated on the basis of the experimental results. The roles of Ce, Sn and $LaMnO_3$ were also discussed in this study.

1. Introduction

Elemental mercury (Hg^0) emitted from coal-fired power plants is hazardous pollutant in the atmosphere.[1–3] Hg^0 is hardly removed due to its insolubility in water and high volatility.[4] Currently, the efficient methods for the removal of Hg^0 make full use of the existing air pollution control devices (APCDs) to remove Hg^0 and NO_x/particles/SO_2.[2,5] In general, catalytic oxidation and adsorption are two primary mechanisms for Hg^0 removal. Hg^0 transformed to oxidized state (Hg^{2+}) by catalytic oxidation could be easily removed in the wet flue gas desulfurization (WFGD) system. Hg^0 changed to particle-bound mercury (Hg^p) can be captured by dust-cleaning apparatus. In the dust cleaning process, the catalytic oxidation of Hg^0 to Hg^{2+} was also beneficial for chemical adsorption. Therefore, catalytic oxidation of Hg^0 to Hg^{2+} was the key to controlling Hg^0 emission.

Among the catalysts or sorbents in recent studies, Mn-based metal oxides were proven to be efficient materials for Hg^0 removal from coal-fired flue gas.[6–12] The high redox potential makes them possible for Hg^0 oxidation to Hg^{2+}, along with the adsorption on the surface of materials. In this process, higher catalytic performance and sufficient surface oxygen were beneficial for Hg^0 removal. However, Mn-based metal oxides often suffer two problems for Hg^0 removal: (1) particle aggregation resulted in the low stability, and it is hard to make full use of MnO_x particles; and (2) MnO_x often loses its high activity when the reaction temperature is higher than >200 °C. To solve the first problem, perovskite oxides attracted our attention due to their excellent catalytic oxidation performance. Higher dispersion of Mn ions occupies the B sites in ABO_3 perovskite structure.[13–15] $LaMnO_3$ indicated high Hg^0 removal performance in our recent study. However, it also suffers from low activity at high temperature. In our previous studies, doping of SnO_2 was employed to enhance the Hg^0 removal performance at high temperature.[7,16] Sn–Mn binary metal oxides enlarged the reaction temperature window. In fact, SnO_2 had excellent electron transfer and O_2 capture performance.[17,18] O_2 in the gas can be adsorbed on the surface of SnO_2. Then, the adsorbed O_2 changed to O^{2-} by SnO_2 offering electrons on its surface. The sufficient O^{2-} was favorable for Hg^{2+} capture. In addition, CeO_2 has large oxygen storage capacity and oxygen conversion ability. Ce–Mn mixed metal oxides may have high catalytic oxidation performance because it makes good use of O_2 in the simulated flue gas.[19] Liu *et al.* reported that doping with Ce into SnO_2 increased the surface area, decreased the crystallite sizes, and it showed higher catalytic activity for the catalytic combustion of methane.[18] It was interesting to determine whether Ce–Sn binary metal oxides can be used for Hg^0 catalytic oxidation.

[a]School of Environmental Science and Engineering, Shanghai Jiao Tong University, Shanghai 200240, China. E-mail: nqyan@sjtu.edu.cn; Fax: +86 21 54745591; Tel: +86 21 54745591

[b]Henan Collaborative Innovation Center of Environmental Pollution Control and Ecological Restoration, Zhengzhou University of Light Industry, No. 136, Science Avenue, Zhengzhou 450001, China

† Electronic supplementary information (ESI) available: The detailed information about materials characterization can be found. See DOI: 10.1039/c6ra10006f

In view of the complete perovskite structure, LaMnO$_3$ had higher catalytic performance. Ce–Sn binary oxides were impossible to dope into the perovskite crystal lattice. To date, few reports have discussed the Ce–Sn binary metal oxides used as catalyst supports. In this study, we first optimized the Ce–Mn binary oxides for Hg^0 removal. Subsequently, the Ce–Mn binary oxides were used as a catalyst support for LaMnO$_3$. The performances for Hg^0 removal over these as-prepared materials were evaluated in a fixed-bed adsorption system. The roles of LaMnO$_3$ and the Ce–Sn support were discussed in our study. On this basis, the relationship between the active center and catalyst support was also discussed by physico-chemical characterization. The possible Hg^0 removal mechanism, as well as the application prospect, was proposed accordingly.

2. Experimental section

2.1 Materials preparation and characterization

Ce$_{1-x}$Sn$_x$O$_2$ (x = 0.1, 0.3, 0.5, 0.7, and 0.9) supports were prepared by a co-precipitation method. Suitable amounts of Ce(NO$_3$)$_4$ and SnCl$_4$ dissolved in distilled water. A stoichiometric amount of ammonia was added to the mixture as the precipitation agent under strong stirring for 2 h. The precipitate was then filtered and washed with deionized water three times to remove Cl$^-$ from the water. Lastly, the precipitate was transferred to a muffle furnace and calcined at 500 °C for 5 h. All the samples used as catalysts were ground to a 40–60 mesh size.

Ce$_{1-x}$Sn$_x$O$_2$ was selected as a catalyst support for LaMnO$_3$. The prepared Ce$_{1-x}$Sn$_x$O$_2$ supports were ground to <100 mesh size. The LaMnO$_3$/Ce$_{1-x}$Sn$_x$O$_2$ was prepared using a sol–gel method. The required amount of La(NO$_3$)$_3$ and Mn(NO$_3$)$_3$ was dissolved together in Ce$_{1-x}$Sn$_x$O$_2$ solution, followed by addition of citric acid (CA) in the mixed solution. The temperature of the aqueous solution was maintained constant at 80 °C. The molar ratio for each component was La/Mn/CA = 1 : 1 : 2. After vigorous stirring and evaporation, a transparent gel was formed, which was then dried at 90 °C overnight. The obtained precursor was first calcined at 400 °C for 1 h in air to decompose citric acid totally and was then calcined at 750 °C for 5 h with a rate of 10 °C min^{-1}. All the samples were grounded to 40–60 mesh.

The as-prepared materials were characterized by means of BET surface area measurements, XRD, Raman spectroscopy, H$_2$-TPR and XPS. The detail analysis can be found in ESI.†

2.2 Activities test

The performance for Hg^0 removal over the as-prepared materials was evaluated using a fixed-bed reactor. A Hg^0 permeation tube was used to generate Hg^0 vapor carried by pure N$_2$, which was introduced to the inlet of the gas mixer. Other gases such as O$_2$ were introduced to the gas mixer at constant flows. The mass flow rate was controlled by mass flow controllers (MFC). A fixed-bed reactor system was used to investigate the Hg^0 adsorption performance. The reaction temperature was controlled from 100 to 350 °C using a temperature controller tubular furnace. In each test, the as-prepared materials were placed into the

reaction tube, which was placed to control the reaction temperature. The cold vapor atomic absorption spectroscopy (CVASS) analyzer was used as the online continuous detector. The concentration of Hg^0 was calculated by Lumex RA 915+. The inlet concentration of Hg^0 was 500 ± 50 μg m^{-3}. At the beginning of each test, the simulated gas bypassed the reactor and the inlet gas was detected to ensure a stable Hg^0 concentration. The simulated gas passed the samples and the Hg^0 concentration was detected by CVASS online. The mass of the material for each test was 30 mg.

The Hg^0 removal efficiency was calculated according to eqn (1):

$$\eta_x = \frac{Hg_{in}^0 - Hg_{out}^0}{Hg_{in}^0} \tag{1}$$

where η_x is the removal efficiency, Hg$_{in}^0$ is the inlet concentration of Hg^0, and Hg$_{out}^0$ is the outlet concentration of Hg^0; the reaction time was 600 min for each test.

2.3 Hg-TPD method

Mercury temperature programmed desorption (Hg-TPD) method was built to evaluate the desorption performance of the as-prepared materials. Before each test, the sorbents were first under adsorption for 20 min at 150 °C with 4% O$_2$ balanced with N$_2$ (total flow rate = 500 mL min^{-1}). After the furnace was cooled to 100 °C, the materials were regenerated by heating from 100 °C to 700 in a pure N$_2$ carrier gas. The heating rate was set as 5 °C min^{-1}. The mercury signal was recorded by CVASS online system.

3. Results & discussion

3.1 Hg^0 removal performance

3.1.1 Hg^0 removal performance over Ce$_{1-x}$Sn$_x$O$_2$ mixed oxides. The activities of Ce$_{1-x}$Sn$_x$O$_2$ mixed oxides are shown in Fig. 1. CeO$_2$ showed nearly no activities for Hg^0 removal at 100–
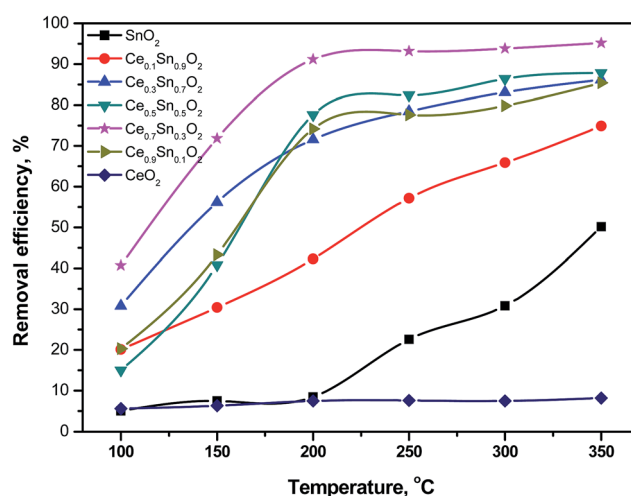
Fig. 1 Hg^0 removal efficiencies of the Ce$_{1-x}$Sn$_x$O$_2$ mixed oxides. Mass of catalyst: 30 mg; total flow rare: 500 mL min^{-1}; gas components: 4% O$_2$; reaction time: 600 min.

350 °C. For SnO$_2$, it exhibited no activities when the temperature was less than 200 °C. However, the removal efficiencies were enhanced when the temperature was higher than 200 °C. The Hg^0 removal efficiency was approximately 50% when the temperature was 300 °C. The results indicated that SnO$_2$ had high catalytic activity at high temperatures. SnO$_2$ could adsorb O$_2$ in the simulated gas to form O^{2-} on the its surface, which was beneficial for Hg^0 oxidation.[20,21] For Ce$_{1-x}$Sn$_x$O$_2$ mixed oxides, they all showed high activities compared with pure SnO$_2$. Ce$_{0.1}$Sn$_{0.9}$O$_2$ enhanced about 30% Hg^0 removal efficiencies; the highest removal efficiency was higher than 70% at 350 °C. Among the mixed oxides, Ce$_{0.7}$Sn$_{0.3}$O$_2$ showed the best Hg^0 removal performance. The Hg^0 removal efficiency was about 90% at 200 °C and the highest removal efficiency was 95.2% at 350 °C. Ce$_{0.3}$Sn$_{0.7}$O$_2$, Ce$_{0.5}$Sn$_{0.5}$O$_2$ and Ce$_{0.9}$Sn$_{0.1}$O$_2$ showed similar performances for Hg^0 removal. Based on these results, Ce$_{1-x}$Sn$_x$O$_2$ mixed oxides enhanced the Hg^0 removal efficiency significantly. Among the Ce–Sn binary oxides, Ce$_{0.7}$Sn$_{0.3}$O$_2$ showed the highest activities for Hg^0 oxidation.

3.1.2 Hg^0 removal performance using Ce$_{0.7}$Sn$_{0.3}$O$_2$ as catalyst support. It was indicated that Ce$_{0.7}$Sn$_{0.3}$O$_2$ had the highest activity for Hg^0 removal. Ce$_{0.7}$Sn$_{0.3}$O$_2$ was used as a catalyst support for the modification of LaMnO$_3$. For comparison, the Hg^0 removal performance of LaO$_x$/Ce$_{0.7}$Sn$_{0.3}$O$_2$ and MnO$_x$/Ce$_{0.7}$Sn$_{0.3}$O$_2$ were also tested. The reaction temperature was set to 150 °C because the material used for Hg^0 adsorption is usually in the dust removal unit wherein the temperature ranged from 100 to 200 °C. As shown in Fig. 2, the performance of LaO$_x$/Ce$_{0.7}$Sn$_{0.3}$O$_2$, MnO$_x$/Ce$_{0.7}$Sn$_{0.3}$O$_2$ and LaMnO$_3$/Ce$_{0.7}$Sn$_{0.3}$O$_2$ was different. LaO$_x$/Ce$_{0.7}$Sn$_{0.3}$O$_2$ had almost no activity for Hg^0 removal. MnO$_x$/Ce$_{0.7}$Sn$_{0.3}$O$_2$ had the highest Hg^0 removal efficiency (~80%) at the initial minutes. However, it lost the activity gradually and it completely had no activity until the reaction time was 600 min. Among these three materials, LaMnO$_3$/Ce$_{0.7}$Sn$_{0.3}$O$_2$ had the best performance for Hg^0 removal. The Hg^0 removal efficiency was higher than 90%
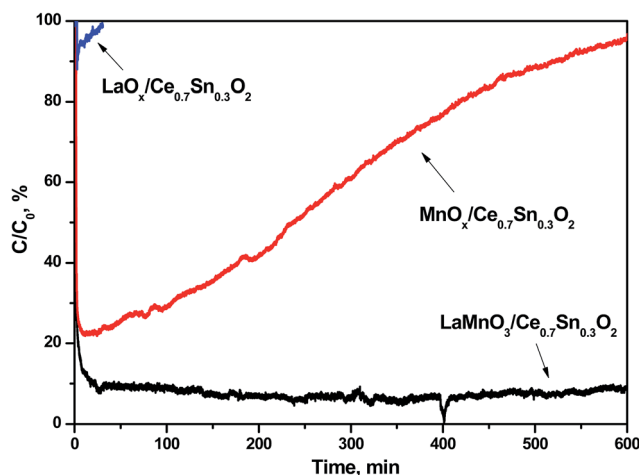
even after a 600 min reaction. This indicates that the perovskite crystal structure was beneficial for Hg^0 oxidation. In previous studies, the perovskite oxides had been proven to have high catalytic oxidation performance.[14] The Hg^0 removal mechanism over LaMnO$_3$ perovskite oxides would be discussed in the following section.

To further identify the effects of the Ce$_{0.7}$Sn$_{0.3}$O$_2$ catalyst support for LaMnO$_3$ on the Hg^0 removal efficiency, the performances of LaMnO$_3$/CeO$_2$, LaMnO$_3$/SnO$_2$ and LaMnO$_3$/Ce$_{0.7}$Sn$_{0.3}$O$_2$ were evaluated at a wide temperature window. As shown in Fig. 3, LaMnO$_3$/CeO$_2$ had the highest Hg^0 removal efficiency (94.5%) at 150 °C, while the removal efficiency decreased to only 38.5% when the temperature was increased to 300 °C. Higher temperatures resulted in low activity over Mn-based material. However, when SnO$_2$ acted as catalyst support for LaMnO$_3$, the Hg^0 removal efficiency increased, especially at high temperatures (>200 °C). The Hg^0 removal efficiency was 85.63% at 250 °C, which was higher than that compared with 50.3% of LaMnO$_3$/CeO$_2$ at the same temperature. For LaMnO$_3$/Ce$_{0.7}$Sn$_{0.3}$O$_2$, the performance was further enhanced compared to that of LaMnO$_3$/SnO$_2$. The Hg^0 removal efficiency was greater than 90% even when the temperature was as high as 250 °C, and the Hg^0 removal efficiency can maintain about 60% at 300 °C. These results indicated that SnO$_2$ support can enlarge the reaction temperature window and Ce$_{0.7}$Sn$_{0.3}$O$_2$ acted as LaMnO$_3$'s support showed excellent Hg^0 removal performance.

3.1.3 Effects of O$_2$, SO$_2$ and H$_2$O on LaMnO$_3$/Ce$_{0.7}$Sn$_{0.3}$O$_2$. As shown in Fig. 4, the effects of various gas components on Hg^0 removal efficiencies over LaMnO$_3$/Ce$_{0.7}$Sn$_{0.3}$O$_2$ were investigated. The reaction temperature was 150 °C and the reaction time was 600 min. It was obvious that the Hg^0 removal efficiency was dropped by about 40% under pure N$_2$ compared to 4% O$_2$. When there was 8% O$_2$ in the simulated gas, the Hg^0 removal efficiency increased. This indicates that O$_2$ participated in the reaction, O$_2$ acted as oxidant for Hg^0 oxidation.[22] The effects of

Fig. 2 Hg^0 removal efficiencies of LaO$_x$/Ce$_{0.7}$Sn$_{0.3}$O$_2$, MnO$_x$/Ce$_{0.7}$Sn$_{0.3}$O$_2$ and LaMnO$_3$/Ce$_{0.7}$Sn$_{0.3}$O$_2$. Mass of catalyst: 30 mg; total flow rare: 500 mL min^{-1}; gas components: 4% O$_2$; reaction temperature: 150 °C, reaction time: 600 min.
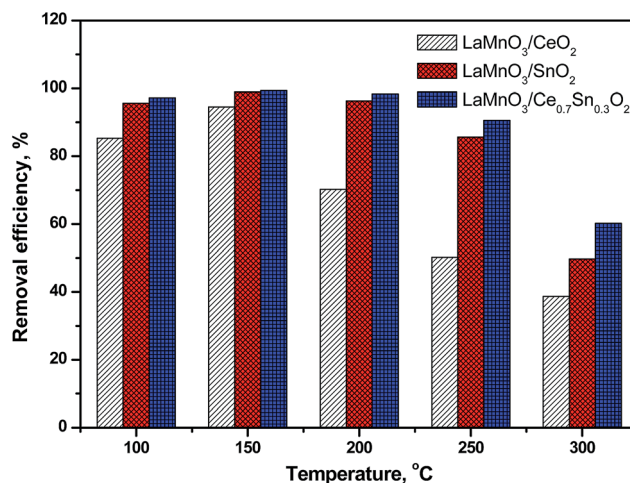
Fig. 3 Hg^0 removal efficiencies of LaMnO$_3$/SnO$_2$, LaMnO$_3$/CeO$_2$ and LaMnO$_3$/Ce$_{0.7}$Sn$_{0.3}$O$_2$ at a wide temperature window (100–300 °C). Mass of catalyst: 30 mg; total flow rare: 500 mL min^{-1}; gas components: 4% O$_2$; reaction temperature: 100–300 °C, reaction time: 600 min.
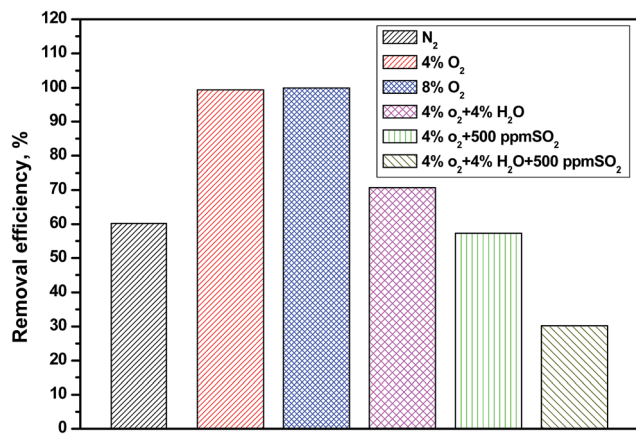
Fig. 4 Effects of O_2, SO_2, and H_2O on the Hg^0 removal efficiencies.

Fig. 5 XRD patterns of (a) $Ce_{1-x}Sn_xO_2$ mixed oxides, and (b) $LaMnO_3/SnO_2$, $LaMnO_3/Ce_{0.7}Sn_{0.3}O_2$ and $LaMnO_3/CeO_2$.

H_2O and SO_2 on Hg^0 removal were also tested. The results showed that 4% H_2O in the simulated gas was unfavorable for Hg^0 removal, the removal efficiency decreased to 70.7%. In addition, 500 ppm SO_2 dropped the Hg^0 removal efficiency. The Hg^0 removal efficiency decreased sharply when 4% O_2 and 500 ppm SO_2 co-existed in the simulated gas. For $LaMnO_3/Ce_{0.7}Sn_{0.3}O_2$, it also suffered from poisoning by SO_2 and H_2O, as well as other Mn-based materials for Hg^0 removal.[16]

3.2 Characterization of the materials

X-ray power diffraction (XRD) was utilized to clarify the crystal phases of the as-prepared $Ce_{1-x}Sn_xO_2$ binary metal oxides and their supported material. As depicted in Fig. 5(a), it showed the XRD patterns of $Ce_{1-x}Sn_xO_2$. For SnO_2, the diffraction peaks of can be well indexed to SnO_2 (JPCDS no. 21-1250). The diffraction peaks of CeO_2 were ascribed to CeO_2 (JPCDS no. 43-1002). With the addition of CeO_2 in SnO_2, the $Ce_{0.1}Sn_{0.9}O_2$ had the CeO_2 phase. However, there were no SnO_2 phases for $Ce_{0.9}Sn_{0.1}O_2$ binary oxides. It could be speculated that the Sn was dispersed on the CeO_2 surface and/or incorporated into CeO_2 lattice.[18] As for the Sn-rich materials, the XRD patterns of the $Ce_{0.1}Sn_{0.9}O_2$ and $Ce_{0.3}Sn_{0.7}O_2$, the patterns existed as a mixed form of CeO_2 and SnO_2. Even for the $Ce_{0.5}Sn_{0.5}O_2$ and $Ce_{0.7}SnO_{0.3}O_2$, the mixing phase co-existed, but the intensity of the SnO_2 phase was not as strong as CeO_2. It could be speculated that, for $Ce_{0.7}Sn_{0.3}O_2$, some of the SnO_2 entered into the lattice of CeO_2 and some of SnO_2 existed on the surface of the mixed metal oxides. Furthermore, as shown in Fig. 5(b), the XRD patterns of $LaMnO_3/CeO_2$, $LaMnO_3/CeO_2$ and $LaMnO_3/Ce_{0.7}Sn_{0.3}O_2$ were also represented. The peaks at 22.8, 32.6, 40.2, 46.7, 52.8, 58.1, 68.3 and 77.8° 2θ, all the characteristic peaks were indexed to a perovskite phase (PDF-88-0633). For $LaMnO_3/CeO_2$, the primary crystal was the perovskite structure. Some peaks can be ascribed to CeO_2.[23] No other peaks were generated on the composite surface. Similarly, the peaks of $LaMnO_3/SnO_2$ had the crystal phase of perovskite oxide and SnO_2. For $LaMnO_3/Ce_{0.7}Sn_{0.3}O_2$, perovskite oxide phase was also the primary crystal structure, $LaMnO_3$ and $Ce_{0.7}Sn_{0.3}O_2$ maintained their respective crystal phase.
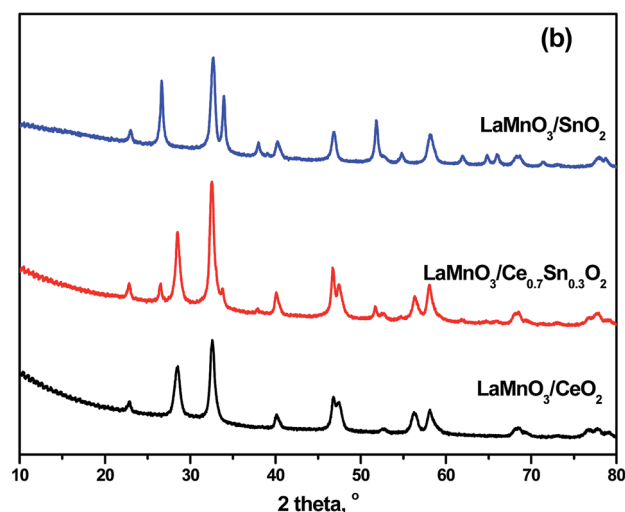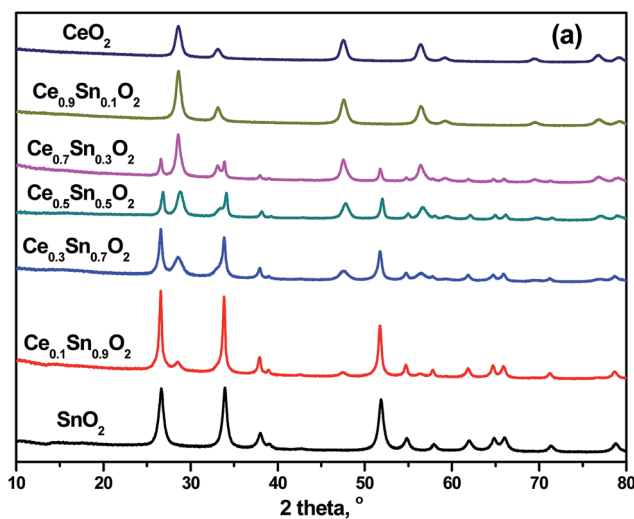
BET analysis was conducted for the as-prepared samples. The BET surface area and the BJH total pore volume are listed in Table 1. Pure $LaMnO_3$ had a surface area of 16.60 m² g⁻¹, which is lower than pure SnO_2 (29.89 m² g⁻¹) and CeO_2 (46.32 m² g⁻¹). For $Ce_{0.7}Sn_{0.3}O_2$, the surface area was 35.74 m², which was

Table 1 BET surface areas and the pore volume of the as-prepared materials

Materials	BET surface area (m² g⁻¹)	BJH pore volume (m³)
$LaMnO_3$	16.60	0.118
SnO_2	29.89	0.141
CeO_2	46.32	0.130
$Ce_{0.7}Sn_{0.3}O_2$	35.74	0.152
$LaO_x/Ce_{0.7}Sn_{0.3}O_2$	74.21	0.625
$MnO_x/Ce_{0.7}Sn_{0.3}O_2$	4.37	0.056
$LaMnO_3/SnO_2$	21.77	0.201
$LaMnO_3/CeO_2$	66.35	0.302
$LaMnO_3/Ce_{0.7}Sn_{0.3}O_2$	86.08	0.434

larger than SnO_2 but smaller than CeO_2. The addition of SnO_2 to CeO_2 increased the pore volume, resulting in a larger surface area. Similarly, the surface area of $LaMnO_3/SnO_2$ (21.77 m^2) was smaller than $LaMnO_3/CeO_2$ (66.35 m^2). However, when $Ce_{0.7}Sn_{0.3}O_2$ acted as the catalyst support, $MnO_x/Ce_{0.7}Sn_{0.3}O_2$ had surface areas of only 4.37 m^2 and a very small pore volume (0.056 m^3). This was the reason why the MnO_x particles was easily aggregated.[8] $LaO_x/Ce_{0.7}Sn_{0.3}O_2$ had a larger surface area of 74.21 m^2 and the larger pore volume of 0.625 m^3. LaO_x can form porous structures combined with Ce–Sn binary oxides. For $LaMnO_3/Ce_{0.7}Sn_{0.3}O_2$, it had the largest surface area (86.08 m^2) among the as-prepared materials. Mn-based oxides often suffer from the problem of particle aggregation. CeO_2 can enlarge the surface area of MnO_x and SnO_2 particles addition could make a larger pore volume, resulting in a larger surface area. The larger surface area was favorable for the Hg^0 reaction on its surface. According to XRD analysis, the $LaMnO_3$ perovskite oxide and Ce–Sn binary oxide maintained had their own crystal structure. The cooperation of them benefited the building the larger pore and the dispersion of Mn-based material.

To reveal the effect of Ce–Sn binary oxide support on $LaMnO_3$, Raman spectroscopy technique was used for structure analysis. For comparison, $LaO_x/Ce_{0.7}Sn_{0.3}O_2$ and $MnO_x/Ce_{0.7}Sn_{0.3}O_2$ were also collected. As shown in Fig. 6, a wide peak at about 500–750 cm^{-1} was observed for $LaMnO_3/SnO_2$. This was attributed to the surface vibrational mode of Sn–O–Sn (A_{1g}) in nanocrystalline SnO_2 and to volume modes of SnO_2.[24] The peak at about 648 cm^{-1} was ascribed to the overlap of MnO_2 with SnO_2.[25] There were no obvious peaks in the $LaMnO_3/CeO_2$ spectrum under the same intensity. With the addition of Sn to the CeO_2 support, the A_{1g} peak widened and vanished due to the presence of bulk oxygen vacancies, resulting in a distortion of the Sn–O bond.[18] The peak at about 461, 462 or 468 cm^{-1} can be ascribed to the F_{2g} vibration mode of CeO_2 in the fluorite structure, the slight shift from 461 to 468 cm^{-1} in the F_{2g} mode was due to nanosize sample.[26] Obviously, MnO_2 overlapped on SnO_2 from the spectrum of $LaMnO_3/Ce_{0.7}Sn_{0.3}O_2$, the addition

of CeO_2 increased more oxygen vacancies.[17] The addition of Sn enhanced the role of MnO_2 which was the main active site for Hg^0 catalytic oxidation. Significantly, the addition of Ce to catalyst support generated more oxygen vacancies, which could enhance the redox ability of the material, resulting in the higher catalytic performance.

The reducibility of the samples was assessed by H_2-TPR. Fig. 7 shows the qualitative profiles recorded over the as-prepared materials. For $LaO_x/Ce_{0.7}Sn_{0.3}O_2$, it presented a wide peak centered at about 531.1 °C. In general, Sn^{4+} can be only reduced to Sn^{2+} below 500 °C, and Sn^{2+} reduced to Sn^0 at the temperature higher than 500 °C. The shoulder peak over $LaO_x/Ce_{0.7}Sn_{0.3}O_2$ could indicate the role of Ce, the reducibility of Ce^{4+} and Sn^{4+} could be promoted simultaneously according to the equilibrium of $Sn^{4+} + 2Ce^{3+} \leftrightarrow Sn^{2+} + 2Ce^{4+}$.[18] $MnO_x/Ce_{0.7}Sn_{0.3}O_2$ presented two character peaks at 488.9 and 595.6 °C, which were assigned to $Mn^{4+} \rightarrow Mn^{3+}$ and $Mn^{3+} \rightarrow Mn^{2+}$, respectively.[27] In the $LaMnO_3/SnO_2$ profile, there were four peaks at 325.2, 547.5, 632.3 and 799.5 °C. The reduction peak of $Mn^{4+} \rightarrow Mn^{3+}$ moved to a lower temperature (325.2 °C). It was speculated that the SnO_2 support was beneficial for the redox of $Sn^{2+} + Mn^{4+} \leftrightarrow Sn^{4+} + Mn^{3+}$. In addition, the peak of $Mn^{3+} \rightarrow Mn^{2+}$ moved to a higher temperature compared to $MnO_x/Ce_{0.7}Sn_{0.3}O_2$. However, with the addition of Ce to the SnO_2 support, for $LaMnO_3/CeO_2$, a wide shoulder peak contributed to $Mn^{4+} \rightarrow Mn^{3+} \rightarrow Mn^{2+}$ at temperatures lower than 500 °C. Moreover, in the spectrum of $LaMnO_3/Ce_{0.7}Sn_{0.3}O_2$, two peaks at 344.8 and 530.4 °C can be ascribed to $Mn^{4+} \rightarrow Mn^{3+}$ and $Mn^{3+} \rightarrow Mn^{2+}$, respectively.[28] The reduction of $Mn^{4+} \rightarrow Mn^{3+}$ was beneficial for Hg^0 oxidation. Ce–Sn binary oxides improved the reducibility compared with $MnO_x/Ce_{0.7}Sn_{0.3}O_2$.

Based on the H_2-TPR results, it indicated that the perovskite structure ($LaMnO_3/Ce_{0.7}Sn_{0.3}O_2$) showed higher reducibility than pure $MnO_x/Ce_{0.7}Sn_{0.3}O_2$, which was beneficial for catalytic oxidation. Furthermore, Sn^{2+} can easily offer electrons, which
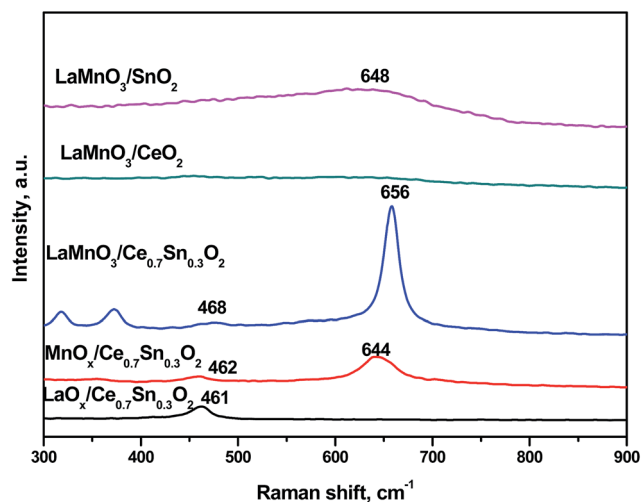
Fig. 6 Raman spectra of $LaO_x/Ce_{0.7}Sn_{0.3}O_2$, $MnO_x/Ce_{0.7}Sn_{0.3}O_2$, $LaMnO_3/Ce_{0.7}Sn_{0.3}O_2$, $LaMnO_3/SnO_2$, and $LaMnO_3/CeO_2$.
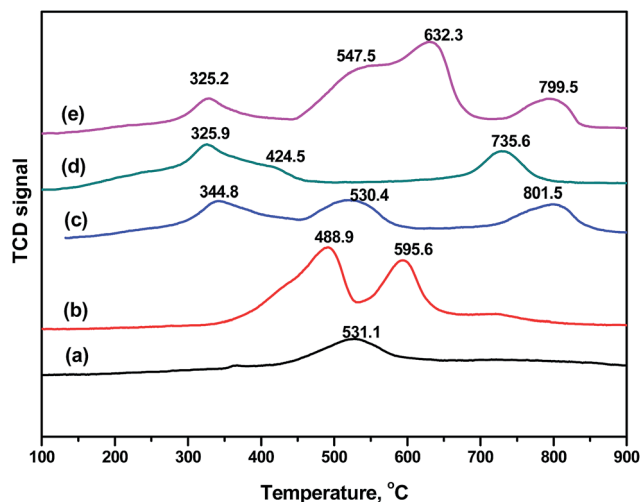
Fig. 7 H_2-TPR profile of the as-prepared materials: (a) $LaO_x/Ce_{0.7}Sn_{0.3}O_2$, (b) $MnO_x/Ce_{0.7}Sn_{0.3}O_2$ and (c) $LaMnO_3/Ce_{0.7}Sn_{0.3}O_2$, (d) $LaMnO_3/CeO_2$, (e) $LaMnO_3/SnO_2$.

also can enhance the reducibility of Mn^{4+} to Mn^{3+}. The addition of Ce enhanced the reducibility of SnO_2 and MnO_x. It was speculated that the reduction of $Mn^{4+} \rightarrow Mn^{3+} \rightarrow Mn^{2+}$ can be enhanced by $Sn^{2+} \rightarrow Sn^{4+}$ or $Ce^{2+} \rightarrow Ce^{3+} \rightarrow Ce^{4+}$. CeO_2 and SnO_2 can also interact with each other. The interaction among the catalytic support and active sites resulted in high catalytic oxidation performance.

To discuss the Hg^0 removal mechanism over $LaMnO_3/Ce_{0.7}Sn_{0.3}O_2$, the XPS spectra of O, Mn and Hg over the fresh and after adsorption of $LaMnO_3/Ce_{0.7}Sn_{0.3}O_2$ are shown in Fig. 8. For the fresh $LaMnO_3/Ce_{0.7}Sn_{0.3}O_2$ sample, Fig. 8(a) shows two peaks of O 1s at 531.1 and 529.6 eV, which corresponded to the adsorbed surface oxygen (O_{ads}) and the lattice oxygen (O_{latt}), respectively.[8] The O_{ads}/O_{latt} ratio was 51.04/48.96.
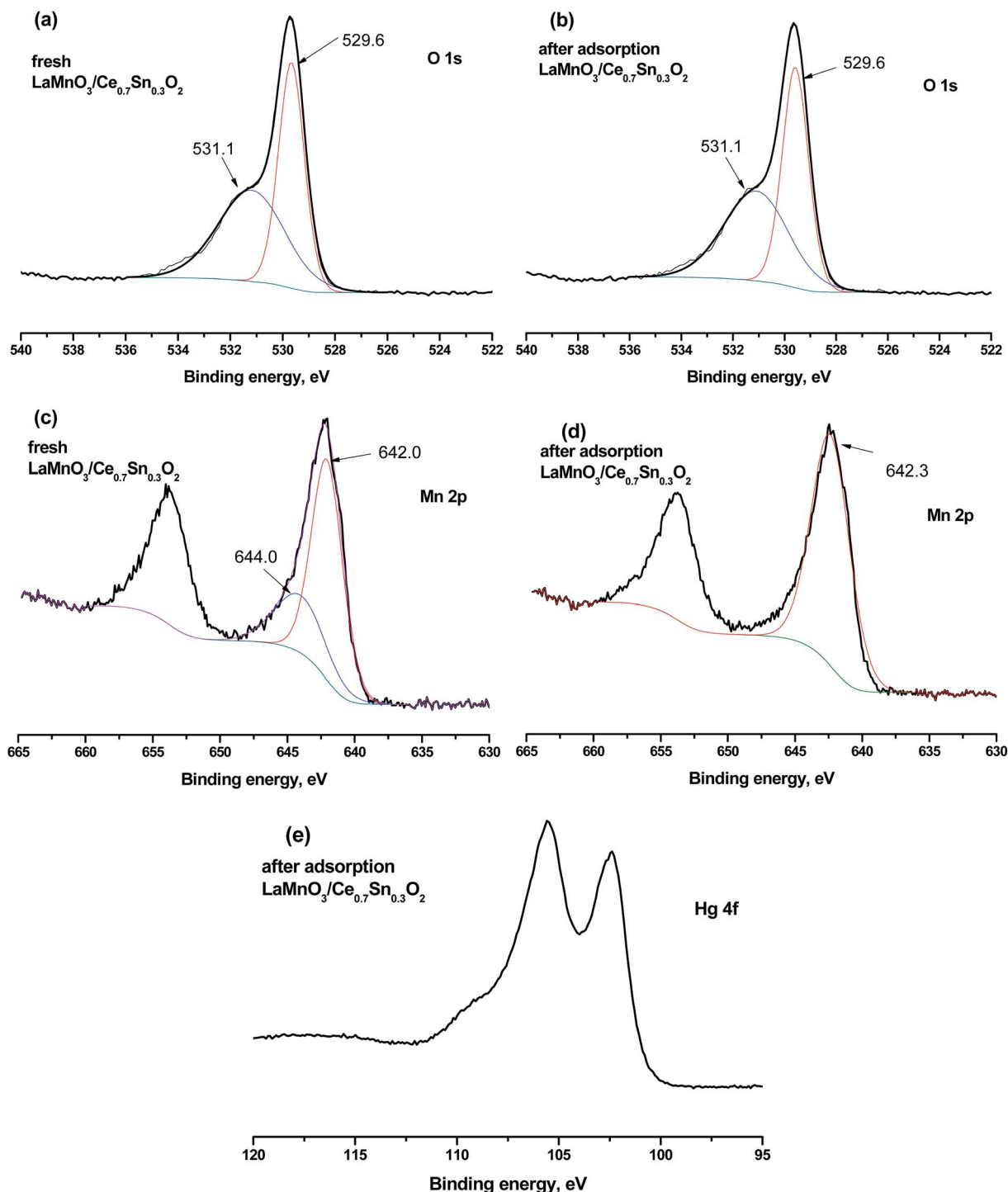
Fig. 8 XPS spectra of $LaMnO_3/SnO_2$ in the O 1s region: (a) fresh sample and (b) after adsorption sample; Mn 2p region: (c) fresh sample and (d) after adsorption sample; and Hg 4f region: (e) after adsorption sample.

After adsorption, as shown in Fig. 8(b), two peaks were detected at the same position over the used $LaMnO_3/Ce_{0.7}Sn_{0.3}O_2$ sample. However, the ratio of O_{ads}/O_{latt} decreased to 49.98/50.02. The surface oxygen was more active than the lattice oxygen based on previous studies.[28] The oxygen took part in the Hg^0 oxidation process, which is in agreement with the experiment results.

Fig. 8(c) displays the Mn 2p XPS spectra over the fresh $LaMnO_3/Ce_{0.7}Sn_{0.3}O_2$ sample, the double main peaks were ascribed to Mn $2p_{1/2}$ and Mn $2p_{3/2}$. Based on the analysis, the fitting peaks at 644.0 and 642.0 were ascribed to Mn^{4+} species and Mn^{3+} species, respectively.[8] No peak could be fitted to Mn^{2+} by analysis calculation. The ratio of Mn^{4+}/Mn^{3+} was 31.88/68.12. The previous studies indicated that the higher valance of Mn, the higher the catalytic oxidation for Hg^0.[28] MnO_2 was considered the primary phase of Mn-based material for Hg^0 oxidation. After adsorption, as the spectra shown in Fig. 8(d), it was interesting that, there was only one fitting peak at 642.3 eV, which corresponded to Mn^{3+}. Obviously, the used material lost Mn^{4+} species due to the reduction of Mn^{4+} to Mn^{3+} ($Mn^{4+} + e^- \rightarrow Mn^{3+}$).

In addition, the Hg 4f spectra of the used $LaMnO_3/Ce_{0.7}Sn_{0.3}O_2$ sample were shown in Fig. 8(e). Two character peaks at 100 to 110 eV can be ascribed to Hg–O on the surface of the material.[29] This further indicated that the mercury removal process was primarily due to chemical adsorption.

The Hg-TPD curves were collected to present the property of mercury binding on the surface of $LaMnO_3$-based material. As shown in Fig. 9, the Hg-TPD curves were collected under 5 °C min⁻¹. The desorption peaks of $LaMnO_3/SnO_2$ and $LaMnO_3/CeO_2$ were centered at 371.4 and 342.3 °C, respectively. Without CeO_2 or SnO_2 as the catalyst support, the desorption peak of $LaMnO_3$ was at 360.8 °C. However, it was obvious that the desorption peak of $LaMnO_3/Ce_{0.7}Sn_{0.3}O_2$ was quite different. There were two peaks at about 300.0 and 697.5 °C, suggesting that two forms of mercury combined with $LaMnO_3/Ce_{0.7}Sn_{0.3}O_2$. The higher desorption temperature indicated stronger interaction forces between the mercury and adsorption sites. The definite bonding styles of mercury can be calculated based on the first-principle theory, which will be performed in our further study. The Hg-TPD results also provided us regeneration method for mercury desorption.

3.3 Hg^0 removal mechanism over $LaMnO_3/Ce_{0.7}Sn_{0.3}O_2$

3.3.1 The role of $LaMnO_3$ perovskite oxide structure. Based on the abovementioned discussions, $LaMnO_3$ was the main active site for Hg^0 removal. In general, Hg^0 removal can be simply described to two steps: first, Hg^0 in the simultaneous flue gas was adsorbed on the surface of $LaMnO_3$, followed by catalytic oxidation of Hg^0 to Hg^{2+}; second, the Hg^{2+} existed on the surface in the form of the Hg–O state. According to the XPS analysis, the mechanism can be explained as follows:

$$Hg^0(g) \rightarrow Hg^0(ads) \quad (2)$$
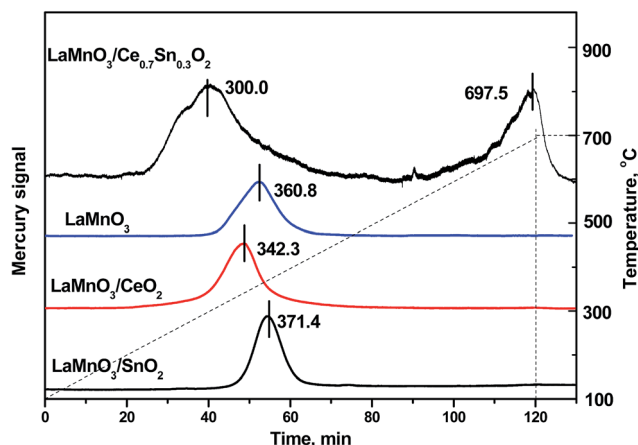
Fig. 9 Hg-TPD curves of $LaMnO_3/SnO_2$, $LaMnO_3/CeO_2$, $LaMnO_3$ and $LaMnO_3/Ce_{0.7}Sn_{0.3}O_2$ at the heating rate of 5 °C min⁻¹.

$$Hg^0(ads) + 2\equiv Mn^{4+} + \equiv O^{2-} \rightarrow 2\equiv Mn^{3+} + \equiv Hg\text{–}O \quad (3)$$
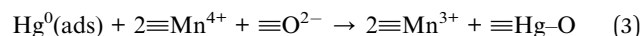
where $\equiv$ represented the adsorption state.

As the active center of the catalyst, $LaMnO_3$ showed high catalytic activity for Hg^0 oxidation due to its special crystal structure.[14] Lanthanum-based perovskite oxides had demonstrated remarkable catalysis performance due to the higher redox behavior, oxygen mobility and ionic conductivity.[30] As illustrated in Fig. 10, oxygen vacancies (where "■" represented oxygen vacancies) can be introduced to the structure to facilitate oxygen transfer and thus increased oxygen mobility.[31] O_2 introduced to oxygen vacancies and formed O^{2-}, which was favorable for Hg^0 oxidation and adsorption. This mechanism also indicated that the Hg^0 removal efficiency decreased when there were no O_2 in the simulated gas.

3.3.2 The role of Ce–Sn binary oxides catalyst support. With the addition of Ce–Sn binary oxides as the catalyst support, the Hg^0 removal performances were enhanced. Based on the physical characterization results, the surface areas were enlarged and the oxygen vacancies were increased. Hg^0 can easily react with the active Mn sites due to the larger surface area. However, the enhancement for Hg^0 removal at
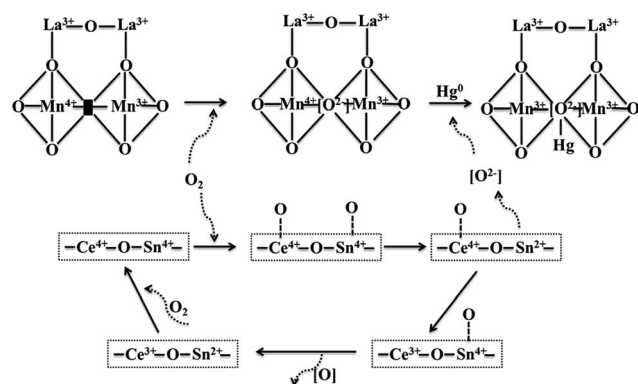
Fig. 10 Possible Hg^0 removal pathways over $LaMnO_3/Ce_{0.7}Sn_{0.3}O_2$ material.

high temperatures should be explained mainly as chemical-adsorption mechanism.

With the addition of SnO_2, the performance at high temperature was enhanced. SnO_2 was believed to be an efficient catalyst that makes full use of O_2 in the simulated gas at high temperatures (>200 °C).[20,21] O_2 in the simulated gas can be adsorbed and exist as physical-adsorption (p-ads) O_2. SnO_2 had super electron transfer performance, which could offer electrons for O_2, the O_2 (p-ads) can be formed O_2^- then to O^- and O^{2-} by getting electrons. The O_2 (p-ads) changed to chemical-adsorption O_2, which was beneficial for Hg^0 capture. During this process, the electrons came from the reduction of Mn^{4+} to Mn^{3+}. The adsorbed O^{2-} on the surface of catalysts was binding site for the oxidized mercury. The mechanism for O_2 transformation can be illustrated as follows:

$$O_2(g) \rightarrow O_2(\text{p-ads}) \quad (4)$$

$$O_2(\text{p-ads}) + e^- \rightarrow O_2^-(\text{c-ads}) \quad (5)$$

$$O_2^-(\text{c-ads}) + e^- \rightarrow 2O^-(\text{c-ads}) \quad (6)$$

$$O^-(\text{c-ads}) + e^- \rightarrow O^{2-}(\text{c-ads}) \quad (7)$$
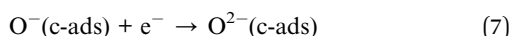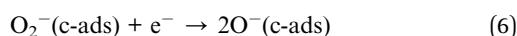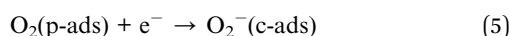
The abovementioned reactions occurred at the temperatures higher than 200 °C. Therefore, the performance of $LaMnO_3$ at high temperatures (>200 °C) can be enhanced after SnO_2 acted as catalyst support.

Moreover, CeO_2 was believed to have high oxygen storage capacity. The adsorbed oxygen can be stored in CeO_2. On the one hand, the sufficient oxygen was beneficial for mercury adsorption. On the other hand, SnO_2 can adsorb O_2 from simulated gas for CeO_2 utilization. In addition, CeO_2 can re-oxidize the reduced Mn (Mn^{3+}) to Mn^{4+}, and Ce_2O_3 can be re-oxidized to CeO_2 by O_2. So the catalyst can be re-used. The equation can be illustrated as follows:

$$2Mn^{3+} + 2CeO_2 \rightarrow 2Mn^{4+} + Ce_2O_3 + \equiv\!O^{2-} \quad (8)$$

$$Ce_2O_3 + 1/2O_2(g) \rightarrow 2CeO_2 \quad (9)$$
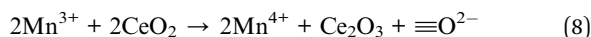
The interaction between Sn and Ce oxides is illustrated in Fig. 10. O_2 in the simulated gas can be captured by Ce–Sn binary oxides when O^{2-} is given to $LaMnO_3$ for the capture of mercury. The reduced Ce (Ce^{3+}) or Sn (Sn^{2+}) can be re-oxidized by the adsorbed-O_2. The catalyst support is regenerated. Furthermore, based on the H_2-TPR results, Ce and Sn also enhanced the reducibility of LaMnO. CeO_2 and SnO_2 benefited the regeneration of reduced Mn. The interaction between Sn, Ce and Mn can be illustrated as follows:

$$Sn^{4+} + 2Ce^{3+} \leftrightarrow Sn^{2+} + 2Ce^{4+} \quad (10)$$

$$Sn^{2+} + Mn^{4+} \leftrightarrow Sn^{4+} + Mn^{3+} \quad (11)$$

$$Ce^{3+} + Mn^{4+} \leftrightarrow Ce^{4+} + Mn^{3+} \quad (12)$$
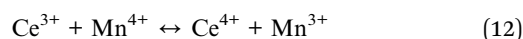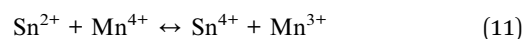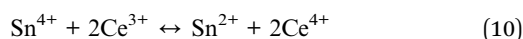
4.   Conclusions

Herein, $Ce_{1-x}Sn_xO_2$ binary metal oxides were synthesized and evaluated for the catalytic oxidation removal of Hg^0. The results indicated that $Ce_{0.7}Sn_{0.3}O_2$ had the best performance for Hg^0 removal. $LaMnO_3/Ce_{0.7}Sn_{0.3}O_2$ presented the highest performance among the as-prepared materials. The surface area was enlarged, the oxygen vacancies were promoted and the reducibility was enhanced when $Ce_{0.7}Sn_{0.3}O_2$ acted as the catalyst support. $LaMnO_3$ were the main active sites for Hg^0 removal, but it lost its activity when the temperature was higher than 200 °C. SnO_2 enhanced the high-temperature performance because it can adsorb O_2 in the simulated gas to generate active O^{2-}. CeO_2 enhanced the oxygen storage capacity and enhanced the catalyst performance. The Ce–Sn catalyst support-modified materials will be a potential catalyst not only for Hg^0 removal, but also for other catalytic oxidation reactions.

Acknowledgements

References

1 Z.-w. Wang, Z.-s. Chen, D. Ning and X.-s. Zhang, *J. Environ. Sci.*, 2007, **19**, 176–180.

2 J. H. Pavlish, E. A. Sondreal, M. D. Mann, E. S. Olson, K. C. Galbreath, D. L. Laudal and S. A. Benson, *Fuel Process. Technol.*, 2003, **82**, 89–165.

3 S. Wang, L. Zhang, G. Li, Y. Wu, J. Hao, N. Pirrone, F. Sprovieri and M. Ancora, *Atmos. Chem. Phys.*, 2010, **10**, 1183–1192.

4 A. L. Soerensen, R. P. Mason, P. H. Balcom, D. J. Jacob, Y. Zhang, J. Kuss and E. M. Sunderland, *Environ. Sci. Technol.*, 2014, **48**, 11312–11319.

5 L. Zhao, C. Li, X. Zhang, G. Zeng and J. Zhang, *Catal. Sci. Technol.*, 2015, **5**, 3459–3472.

6 J. Li, N. Yan, Z. Qu, S. Qiao, S. Yang, Y. Guo, P. Liu and J. Jia, *Environ. Sci. Technol.*, 2009, **44**, 426–431.

7 J. Xie, H. Xu, Z. Qu, W. Huang, W. Chen, Y. Ma, S. Zhao, P. Liu and N. Yan, *J. Colloid Interface Sci.*, 2014, **428**, 121–127.

8 H. Xu, Z. Qu, C. Zong, W. Huang, F. Quan and N. Yan, *Environ. Sci. Technol.*, 2015, **49**(11), 6823–6830.

9 L. Xing, Y. Xu and Q. Zhong, *Energy Fuels*, 2012, **26**, 4903–4909.

10 H. Li, C.-Y. Wu, Y. Li and J. Zhang, *Appl. Catal., B*, 2012, **111**, 381–388.

11 D. Jampaiah, K. M. Tur, P. Venkataswamy, S. J. Ippolito, Y. M. Sabri, J. Tardio, S. K. Bhargava and B. M. Reddy, *RSC Adv.*, 2015, **5**, 30331–30341.

12 D. Jampaiah, S. J. Ippolito, Y. M. Sabri, B. M. Reddy and S. K. Bhargava, *Catal. Sci. Technol.*, 2015, **5**, 2913–2924.

13 S. Cimino, S. Colonna, S. De Rossi, M. Faticanti, L. Lisi, I. Pettiti and P. Porta, *J. Catal.*, 2002, **205**, 309–317.

14 S. Royer, D. Duprez, F. Can, X. Courtois, C. Batiot-Dupeyrat, S. Laassiri and H. Alamdari, *Chem. Rev.*, 2014, **114**, 10292–10368.

15 H. Najjar and H. Batis, *Appl. Catal., A*, 2010, **383**, 192–201.

16 H. Xu, J. Xie, Y. Ma, Z. Qu, S. Zhao, W. Chen, W. Huang and N. Yan, *Fuel*, 2015, **140**, 803–809.

17 H. Chang, X. Chen, J. Li, L. Ma, C. Wang, C. Liu, J. W. Schwank and J. Hao, *Environ. Sci. Technol.*, 2013, **47**, 5294–5301.

18 C. Liu, H. Xian, Z. Jiang, L. Wang, J. Zhang, L. Zheng, Y. Tan and X. Li, *Appl. Catal., B*, 2015, **176**, 542–552.

19 C. He, B. Shen, J. Chen and J. Cai, *Environ. Sci. Technol.*, 2014, **48**, 7891–7898.

20 S. Park, S. An, Y. Mun and C. Lee, *ACS Appl. Mater. Interfaces*, 2013, **5**, 4285–4292.

21 J. Yan, E. Khoo, A. Sumboja and P. S. Lee, *ACS Nano*, 2010, **4**, 4247–4255.

22 Y. Gao, Z. Zhang, J. Wu, L. Duan, A. Umar, L. Sun, Z. Guo and Q. Wang, *Environ. Sci. Technol.*, 2013, **47**, 10813–10823.

23 T. Meng, M. Ara, L. Wang, R. Naik and K. S. Ng, *J. Mater. Sci.*, 2014, **49**, 4058–4066.

24 L. Abello, B. Bochu, A. Gaskov, S. Koudryavtseva, G. Lucazeau and M. Roumyantseva, *J. Solid State Chem.*, 1998, **135**, 78–85.

25 F. Buciuman, F. Patcas and T. Hahn, *Chem. Eng. Process.*, 1999, **38**, 563–569.

26 Z.-Y. Pu, J.-Q. Lu, M.-F. Luo and Y.-L. Xie, *J. Phys. Chem. C*, 2007, **111**, 18695–18702.

27 J. Nie and H. Liu, *J. Catal.*, 2014, **316**, 57–66.

28 H. Xu, Z. Qu, S. Zhao, J. Mei, F. Quan and N. Yan, *J. Hazard. Mater.*, 2015, **299**, 86–93.

29 S. Yang, Y. Guo, N. Yan, D. Wu, H. He, Z. Qu and J. Jia, *Ind. Eng. Chem. Res.*, 2011, **50**, 9650–9656.

30 H. Zhu, P. Zhang and S. Dai, *ACS Catal.*, 2015, **5**(11), 6370–6385.

31 J. T. Mefford, W. G. Hardin, S. Dai, K. P. Johnston and K. J. Stevenson, *Nat. Mater.*, 2014, **13**, 726–732.